A&A 391, 1123–1132 (2002)
DOI: 10.1051/0004-6361:20020873

Astronomy & Astrophysics

Asteroids observations with the Hubble Space Telescope⋆ FGS

I. Observing strategy, and data analysis and modeling process

D. Hestroffer[1,⋆⋆], P. Tanga[2,⋆⋆⋆], A. Cellino[2], F. Guglielmetti[2], M. Lattanzi[2], M. Di Martino[2], V. Zappalà[2], and J. Berthier[1]

[1] IMCCE, UMR CNRS 8028, Observatoire de Paris, 77 Av. Denfert Rochereau, 75014 Paris, France
[2] Osservatorio Astronomico di Torino (OATo), Strada Osservatorio 20, 10025 Pino Torinese (TO), Italy

Received 12 April 2002 / Accepted 28 May 2002

Abstract. Five main belt asteroids and one Trojan – selected mainly on the basis of their possible binary nature as deduced from light curve morphology – have been observed with the Fine Guidance Sensors (FGS#3 and FGSR#1) of the Hubble Space Telescope (HST). In this first paper we present the selection and observation strategy, data reduction and analysis. A careful analysis of the precision for derived parameters is also given. The HST/FGS proves to be valuable in determining asteroid sizes, shapes and spin axis orientations, and also to identify nearly-contact binary systems.

Key words. minor planets, asteroids – methods: observational

1. Introduction

Satellites orbit determination provides a new way to derive the mass (and possibly the bulk density when the volume is also known) of the asteroids. In turn this provides important information on the physical structure and composition of these objects. Since the first suggestions of André 1901) and the original deductions made by Cook (1971) and Tedesco (1979) about the binary nature of (433) Eros, (624) Hektor and (171) Ophelia respectively, theoretical studies on collisions have shown that systems of asteroids may well be described by a small satellite orbiting a minor planet or by near-contact binaries (see e.g. Hartmann 1979; Farinella et al. 1982; Cellino et al. 1985; Weidenschilling et al. 1989; Martelli et al. 1993; Durda 1996; Richardson et al. 1999, and reference therein). Once such a system has been formed, its lifetime can be long, since dynamically stable zones exist (Chauvineau et al. 1991; Leone et al. 1984; Hamilton & Burns 1992; Farinella & Chauvineau 1993). Apart from Earth- or Mars-crossing asteroids (Bottke & Melosh 1996), numerical results (Doressoundiram et al. 1997; Michel et al. 2001) show that the formation of asteroid satellites can be a natural outcome of asteroid collisions. A prediction that is thus in good agreement with the increasing number of satellites detected in recent years, and accrediting the belief of van Flandern et al. (1979) that many asteroids possess satellites.

In fact, after the non-conclusive results of Bowell et al. (1978) and Arlot et al. (1985), and early unsuccessful attempts by Gehrels et al. (1987) and Gradie & Flynn (1988), the existence of binary systems has been spectacularly confirmed by the Galileo discovery of Ida's moon Dactyl (Belton & Carlson 1994; Chapman et al. 1995). Evidence of bifurcated bodies has also been shown by radar observations (Ostro et al. 1990; Ostro 1993; Hudson & Ostro 1994; Benner et al. 1999). More recently, ground-based observations with adaptive optics systems (Merline et al. 1999; Marchis et al. 1999; Merline et al. 2000) or with photometric systems (Pravec et al. 1998; Mottola & Lahulla 2000) have also given positive results. Nevertheless, other recent surveys did not reveal asteroid companions (Roberts et al. 1995; Storrs et al. 1999). For instance, Eros is known to be a single asteroid although its light-curve can be reminiscent of that of an eclipsing binary star. The – up to now – successfully observed binary systems were often detected by chance and there remain many candidates that need further investigation to confirm or not their binary nature. These are often suspected on the basis of light-curve morphology (Cellino et al. 1985) or their unusually long rotation periods (Farinella et al. 1981). High precision astrometry or lunar occultations could also hint the binary nature of some bodies (Hoffmann 1991; Monet & Monet 1998). A good knowledge

Send offprint requests to: D. Hestroffer, e-mail: hestro@bdl.fr

⋆ Based on observations with the NASA/ESA Hubble Space Telescope, obtained at the Space Telescope Science Institute, which is operated by the Association of Universities for Research in Astronomy, Inc. under contract No. NAS5-26555.

⋆⋆ Invited researcher at the Osservatorio Astronomico di Torino OATo.

⋆⋆⋆ Associate researcher at the IMCCE. *Present address*: Laboratoire Cassini, UMR 6529, Observatoire de la Côte d'Azur, BP 4229, 06304 Nice Cedex 4, France.

Table 1. Selected targets, predicted V magnitude, and typical rms noise of the data σ_o (see text).

Name	V mag	σ_o
(15) Eunomia	8.6	0.01
(43) Ariadne	10.3	0.02
(44) Nysa	10.6	0.02
(63) Ausonia	11.7	0.03
(216) Kleopatra	10.8	0.02
(624) Hektor	15.0	0.13

of the physical properties of such systems, their relative frequency, dynamical properties, etc. is of great importance to shed light on the accretion history and collisional evolution of the asteroids in the main belt and hence on the formation and evolution of our Solar System. In addition, high resolution direct or synthetic imaging observations, even when they do not reveal the binary nature of a given object, do provide useful information on its pole orientation, size, shape, and surface or albedo features.

We present in this first paper the reduction and analysis process for observations performed with the HST/FGS astrometer on selected asteroids. The first section describes the selection and observation process. In the second section we describe the data reduction developed to yield the best possible signal-to-noise ratio (SNR). The next section describes the model used to fit the data and its sensitivity to various free parameters. The results for the whole program of observations will be discussed in a forecoming paper (Tanga et al. in prep.).

2. Observations and data reduction

2.1. Observations

A set of six asteroids was selected for observation with the FGS astrometer during HST Cycle 6 (Tanga et al. 1999). All were suspected of being nearly-contact binaries if not strongly elongated bodies. It is stressed that the aim of this observing program is not to detect a small companion orbiting a minor planet, as is the case for (243) Ida or (45) Eugenia. Small moons do not provide notable features on light-curves, and are probably generated from different physical mechanisms. We are instead looking for similar-sized binary pairs of the type of (4769) Castalia or (90) Antiope (Ostro 1993; Merline et al. 2000), or systems similar to those proposed by, e.g., Pravec et al. (1998) or Mottola & Lahulla (2000) from light-curves, or bi-lobated asteroids like (216) Kleopatra (Marchis et al. 1999; Ostro et al. 2000; Tanga et al. 2001).

The target selected for this HST program (ID 7488, PI V. Zappalà) and listed in Table 1 were chosen on the basis of peculiar photometric properties reminiscent of those of eclipsing binary stars and with large lightcurve amplitude, suggesting a possible binary nature (see Leone et al. 1984; Cellino et al. 1985). Moreover their (single-object) light-curve model sometimes implies such an elongated body that, given the rotation period, it could hardly correspond to a Jacobi ellipsoid in stable equilibrium if not of low bulk density (Weidenschilling 1980; Zappalà et al. 1983).

The observations of (15) Eunomia, (43) Ariadne, (44) Nysa, (63) Ausonia, and (624) Hektor were carried out with the FGS#3 instrument[1] in transfer mode (TRANS), optimizing the balance between an oversampled response function and an adequate SNR per resolution element. As described in the FGS Instrument Handbook[2] (Nelan & Makidon 1999), this operating mode samples the target's interferogram (also called S-curve) produced by a Koester prism in two orthogonal directions called the FGS-X and FGS-Y axes. The clear PUPIL filter produces optimal sensitivity (Lattanzi et al. 1994) and was used for all the targets observed with the FGS#3. For Kleopatra, which was observed with the FGSR#1, the F583W filter was used. This latter filter has the same central wavelength and bandpass as the PUPIL one, but with a substantially higher transmissivity (Nelan & Makidon 1999). In order to improve the detection efficiency of a hypothetical binary system, observations should be carried out when the components are at maximal apparent separation. Beside second-order effects (e.g. albedo features, shadowing and phase effects), this coincides with the largest surface exposed toward the observer, corresponding in turn to a rotational phase close to that of a light-curve maximum.

All the asteroids of this observing program have been extensively observed with photometric techniques in the past yielding rotation period, tri-axial ellipsoid models and solutions for the spin axis orientation. Physical ephemerides were constructed from these models, where the synthetic pole solutions of Magnusson et al. (1994) were retained. In order to construct such ephemerides an origin meridian has to be chosen: it is defined to be one of the two meridians corresponding to the major axis. Next its position is fixed such that the sub-earth point (SEP) longitude is either equal to 90 or 270 degrees at the epoch of a primary or secondary maximum, respectively, as obtained from a particular light-curve[3]. By cross-checking predictions and observations of light-curve maxima observed at a similar aspect angle, it was verified that the observed-minus-calculated residuals are typically of the order of 10 min of time, corresponding to an uncertainty on the rotational phase of about 1–2% for periods in the 5–9 hour range, largely sufficient for our purpose. From this, one can link the apparent-ellipse size and shape at any date to the projected length along the FGS-X or -Y axis. Photometric models, since they are derived from disk-integrated photometry, suffer a pole ambiguity. An image of the projected ellipse can however discriminate wrong pole solutions: as shown in Fig. 1 we see that both the sizes on the FGS axes and their variation in time due to the asteroid rotation are different at the time of observation depending on whether one pole solution or the other is retained.

[1] Due to a technical problem, the asteroid (216) Kleopatra was not observed during the assigned proposal schedule, but in January 2000 with the FGSR#1 instrument.

[2] Accessible at URL: `http://www.stsci.edu/instruments/fgs/handbook/`

[3] Second order effects due to the phase are neglected.

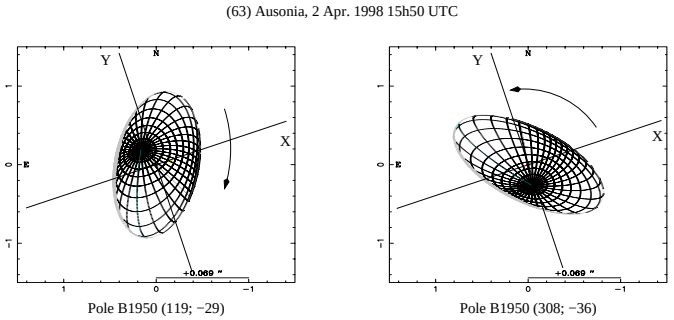

Fig. 1. Physical ephemeris of asteroid (63) Ausonia at a given date of our observational program, and for two pole orientation solutions. The asteroid sens of rotation and the orientation of the FGS axis are given on the figure. Labels are in units of the minor planet semi-major axis.

It has to be noted that in order to minimize the effect of the asteroid proper motion, the epoch chosen is close to the stationary point of each object. In contrast to stars however, solar system objects have a non-negligible parallax. The main contribution to the target apparent motion on the sky is thus given by the orbital motion of the HST platform itself. This effect was modeled and subtracted from the observations as explained below.

2.2. Data reduction

The asteroid apparent motion as seen from HST is due to its displacement relative to the Earth combined with the spacecraft motion on its orbit. Since the HST cannot track a moving object while operating with the FGS in TRANS mode, a change of the transfer function (TF) results. In particular, since the TF is sampled at a uniform speed in the instrument window, the source motion combines with the instrument displacement on the focal plane. Considering the projection of the motion along each FGS axis, the spatial scale of the observed S-curve will be a linear transformation of the scale in which the asteroid is at rest. Calling by $v_{\rm p}$ the velocity of the target projected on the scan direction (one for each FGS axis) and by $v_{\rm s}$ the scan rate, the relation between the observed position along the scan axis (u') and the position that would be observed with a fixed target (u) is given by the scaling:

$$u' = \frac{v_{\rm s}}{v_{\rm s} - v_{\rm p}}\, u; \quad (v_{\rm p} << v_{\rm s}). \tag{1}$$

The values of $v_{\rm p}$ can be computed considering the orientation of the FGS on the sky and the HST orbital motion (both data available from the spacecraft orbitography) and the target ephemeris. Given the motion of HST on its orbit relative to the target direction, for a typical main-belt asteroid (at 2.8 AU from the Sun) near its stationary point, $v_{\rm p}$ can be of the order of 10 mas/s (milli-arcsecond/s). As a consequence, the scale change can be as large as a few percent (and even larger for an inner-belt object with higher parallax). The velocity change during a single scan is small and it has been neglected. Each scan has been processed to remove the target movement effect before any other data reduction. It is stressed that fast-moving objects quickly exit the 2×2 arcsec^2 scan window and require frequent re-acquisition. The FGS acquisition and tracking is made by searching for the object, following a spiral pattern with a final radius of 15 arcsec, and has always been successful.

In order to improve the SNR of the data, a single S-curve is constructed from 4 to 6 consecutive scans (covering approximately 3 min) following the multiple scan merging strategy used by Lattanzi et al. (1997). Briefly, the subsequent scan S-curves are shifted and added to produce a mean S-curve of lower noise. In contrast to Lattanzi et al. (1997) however, no distinction is made between odd and even scans. From now on, we will call "visit" such a normal point observation. This merging process requires the accurate re-centering of each scan S-curve (so that their zero-points coincide) by a shift applied along the spatial axis. This zero-point can easily be determined from a high SNR S-curve. For the fainter object (624) Hektor, of magnitude $V \sim 15$, a polynomial fit of the entire section comprising the S-curve's maximum and minimum provides this zero point. Bad scans due to object loss, excessive telescope jitter, etc. were discarded before merging.

3. Model for a moderately extended source

3.1. Synthetic S-curves

The basic feature of the model is the convolution – for each FGS axis – of the signal of a point-like source (template or TF) with the modeled 2D brightness distribution of the target's contour. Let $T(x)$ be the template transfer function over a given FGS axis. Computation of the signal of a radially symmetric extended target is straightforward when $T(x)$ can be expressed analytically (see Appendix A). Ideally we have for a monochromatic point source $T(x) = -\frac{\sin^2 z}{z}$; where $z = \frac{2\pi R}{\lambda}\, x$ (Nelan & Makidon 1999), and $R = 1.2$ m is the telescope primary-mirror radius. Polychromaticity, aberration and misalignments causes the actual TF to have a different shape. For a target of ellipsoidal shape $\mathcal{E}$ the signal writes:

$$S(x) = \frac{\iint_{\mathcal{E}} I(u,v)\, T(x - u\cos\gamma + v\sin\gamma)\, {\rm d}u\, {\rm d}v}{\iint_{\mathcal{E}} I(u,v)\, {\rm d}u\, {\rm d}v} \tag{2}$$

where γ is the position angle with respect to the FGS axis of the ellipse major-axis and $I(u,v)$ is the brightness distribution over the observed surface (see Appendix B). The equation for a binary system is easily derived from the previous Eq. (2) as a linear combination of two S functions. Since no satisfactory analytical formulation exists for the transfer function of the instrument, calibrated templates made available by the STScI are used. The convolution is thus achieved by numerical integration making use of Gauss' method (Mineur 1952, p. 261) which is well adapted to the integration in Eq. (2). In order to avoid systematic errors, the reference source should match as closely as possible the target spectra and magnitude. Moreover the template acquisition should be taken as close in time as possible to the actual observation and at the same position in the field of view[4]. One should be aware of non negligible – although small – differences in the results with the adopted template for the transfer function (see Fig. 2). This will introduce a bias in

[4] The TF variation over the integration range in Eq. (2) is negligible.

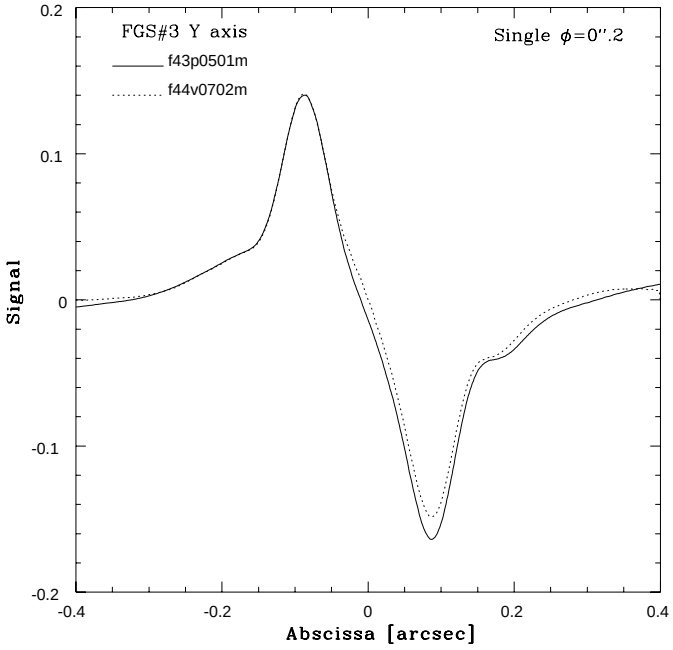

Fig. 2. Comparison of the modeled S-curves for a 0.2 arcsec object and two different available transfer functions.

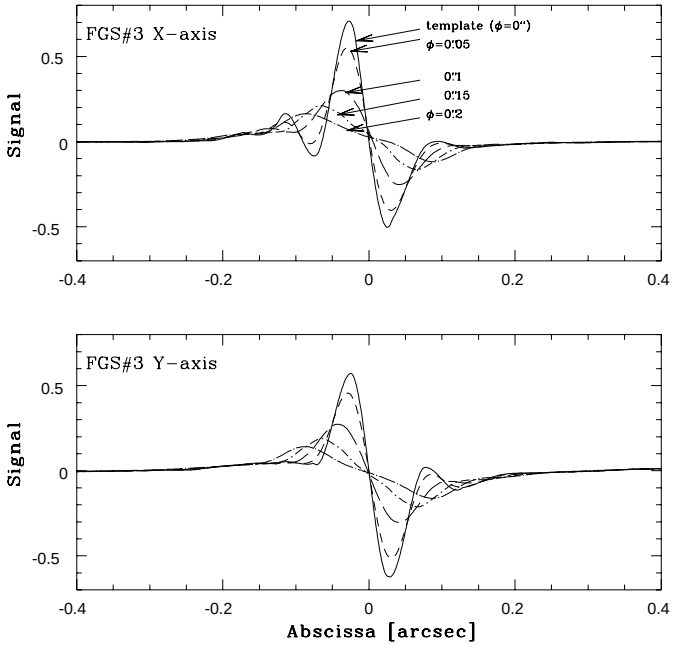

Fig. 3. Computed signal on the X- and Y-axis for a single source with different apparent diameters.

any parameter derived from a fit of this model to any observational data. Results from this numerical procedure were also compared to those from an analytical formulation where the aberrated template TF is computed (Loreggia 1997). The comparison is essentially qualitative but shows nevertheless good agreement. Although the numerical integration could be carried out for any shape and brightness distribution, the target is modeled, at this stage, by a single or double tri-axial ellipsoid. The orientation of the body or the system in space can be arbitrary; in the case of a binary system, however, the mutual shadow has not been taken into account at this stage, since it can be neglected to a first approximation for observations made at phase angles of about 20°, typical of main-belt objects near quadrature.

3.2. Effects of size and duplicity

The FGS astrometer offers many observation capabilities (Nelan et al. 1998) that have already been used in the past for binary stars (Franz et al. 1991, 1992; Bernacca et al. 1993, 1995; Schneider et al. 1998), extended Miras (Lattanzi et al. 1994, 1997) and AGN (Hook et al. 2000). For such objects the fringe pattern or S-curve changes with respect to that of a point-like source. The same happens when considering resolved asteroids. A typical apparent size for a 100–200 km large main-belt asteroid is 0.1–0.2 arcsec with a magnitude of $V \sim 12$. Synthetic S-curves are shown in Fig. 3 for various apparent diameters and Fig. 4 for binary systems. One notes that in the case of a contact or nearly-contact binary of relatively large components, a very particular feature clearly appears near the abscissae origin. This is further amplified when the component separation is increased (see Fig. 5). It clearly appears that the FGS is a good instrument to detect or confirm binary systems among asteroids, but also to investigate their

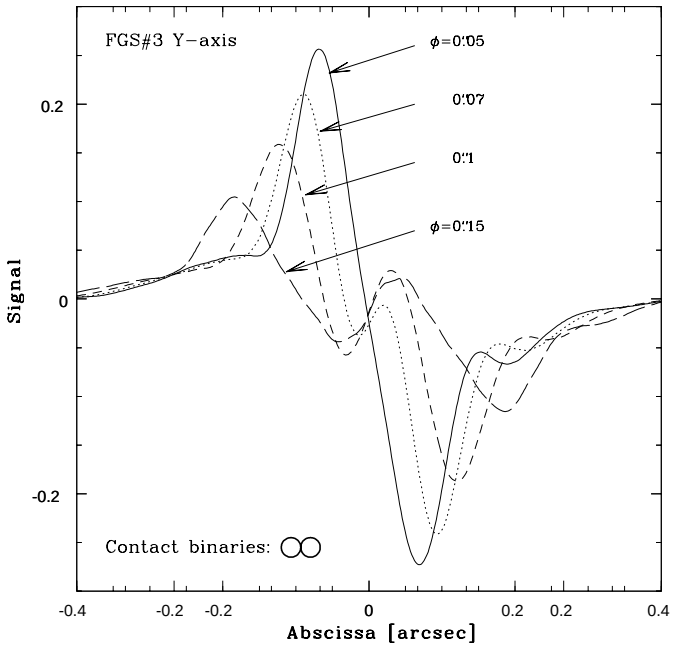

Fig. 4. Computed signal on the Y-axis for a contact binary made of two identical components. Curves are given for various apparent diameters and an along-axis view.

size and shape. On the other hand, given the photon noise for a typical main-belt asteroid, our simulations show that the FGS would hardly detect asteroid moons fainter by approximately 1.5–2 mag than the primary and at separations of the order of the main body Hill radius. Thus the FGS is neither adapted to the detection nor to the observation of small satellites of asteroids (e.g. Eugenia, Pulcova), but to binary systems were the secondary is at least half the size of the primary.

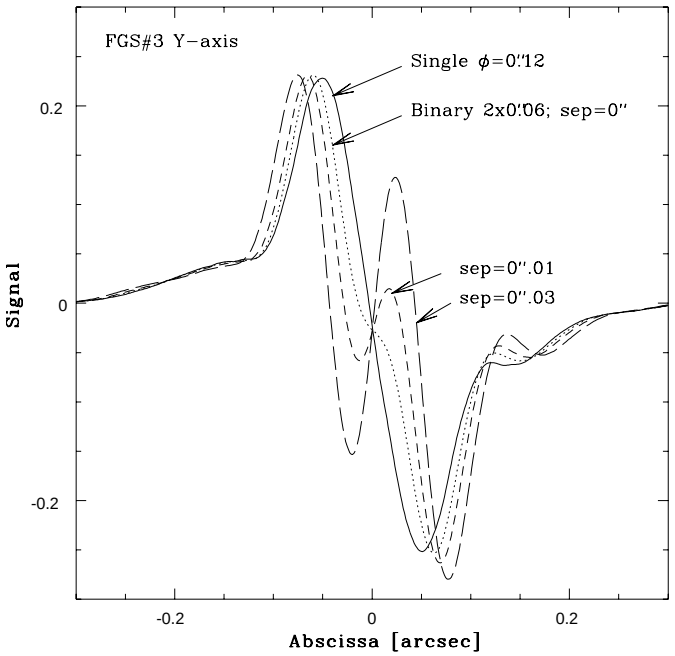

Fig. 5. Computed signal on the Y-axis for a binary of two identical $\phi = 0.06$ arcsec components. The solid curve is given for a single object of diameter $\phi = 0.12$ arcsec, the other curves are given for various separations and an along-axis view.

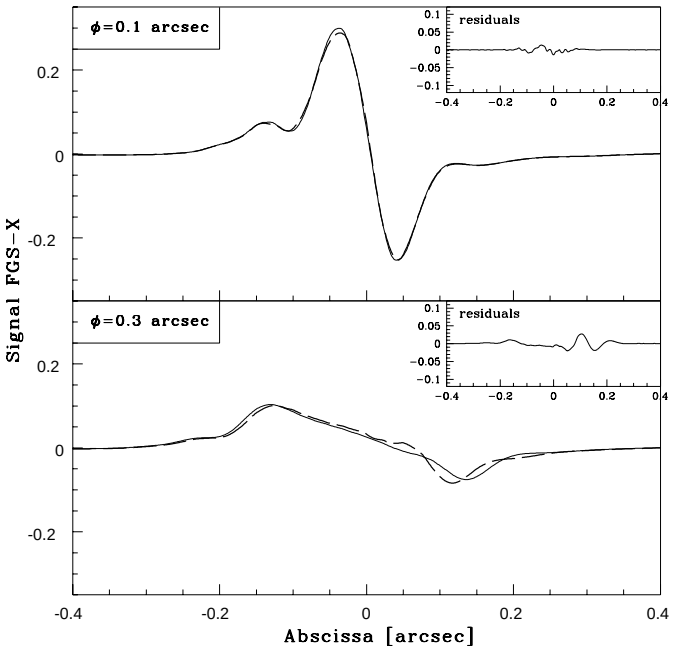

Fig. 6. Influence of a dark spot on the target surface. Plots of the synthetic S-curves (solid lines) are given for two target diameters: 0.1 arcsec (top) and 0.3 arcsec (bottom). The spot location ($\lambda = \pi$, $\beta = 0$) in the ellipsoid's principal axis frame, albedo (0.2) and relative size (60 degrees angular radius) are unchanged. The best-fit solutions are also plotted (dotted lines).

3.3. Effects of shape, phase and limb-darkening

In contrast to a typical extended star, asteroids can be very elongated (with a flattening of the order of 0.4), present a relatively large phase when observed close to the quadratures and may well present a center-to-limb darkening. We show, however, that at the given observation geometry these parameters have a second-order relevance for the shape of the observed S-curve. This means that the FGS instrument essentially measures the size of the object projected on the scan directions. The flattening and orientation of the apparent ellipse has no effect on the modeled signal for a uniformly bright object (see Appendix C for a proof). The effect is still negligible in the more general case when the observed surface presents a limb-darkening. Three simple classes of brightness distributions are considered, (U) uniform brightness, (M) Minnaert's law (Minnaert 1941), and (B) Buratti's law (Buratti & Veverka 1983):

$$\begin{aligned} &\text{U: } I(\mu, \mu_o) = 1 \\ &\text{M: } I(\mu, \mu_o) = \mu_o^k \mu^{k-1} ; \qquad (1/2 \le k \le 1) \\ &\text{B: } I(\mu, \mu_o) = (1-A)\frac{\mu+\mu_o}{\mu_o} + A\,\mu_o ; \quad (0 \le A \le 1) \end{aligned} \tag{3}$$

where μ_o and μ are the cosines of the angles between the surface normal and respectively the incident and reflected ray. Minnaert's $k = 1$ and Buratti's $A = 1$ correspond to a limb darkening following Lambert's law. More refined models could be introduced but we shall see later that they would not improve the results (see Sect. 4.2.2).

The phase effect is also taken into account in the model. For solar phase angles up to 30 degrees, its influence remains small. Neglecting it, however, would introduce a bias in the derived along-scan size: the signal of a disk of diameter ϕ with a phase $\alpha < 30$ degrees is very close to that of a fully illuminated disk of diameter $\phi\,(1 + \cos\alpha)/2$.

3.4. Effects of dark spots

Presence of a dark (or bright) spot on the target surface can also be included in the model. The main feature obtained, depending on the position of the spot, is an asymmetric S-curve. The effect however increases with larger target diameters. Figure 6 shows an example for a dark disk on the surface of a 0.1 arcsec and 0.3 arcsec diameter sphere. In both cases the spot has the same relative size and position. In a similar way to the solar phase, the presence of a non-modeled dark spot can bias the resulting estimated diameter. For the 0.1 arcsec sphere a reasonable fit is obtained with no spot but a 20% larger diameter. For the better-resolved 0.3 arcsec diameter, the best-fit solution is obtained with a 17% larger diameter, but the residuals clearly show the un-modeled effect.

In the simple model only a tri-axial ellipsoid is considered, but this can be extended to "egg-shaped" bodies with the following Cartesian transformation:

$$\begin{aligned} X &= x \\ Y &= y\,\frac{b}{a}\,(1 + \xi\, x) \end{aligned} \tag{4}$$

where ξ is a parameter defining the departure from the apparent ellipsoid. In this case, as shown in Fig. 7, the S-curve becomes asymmetric, as does the light-curve. The size of the effect depends on ξ, on the body's size, and on the figure's orientation with respect to the FGS axis.

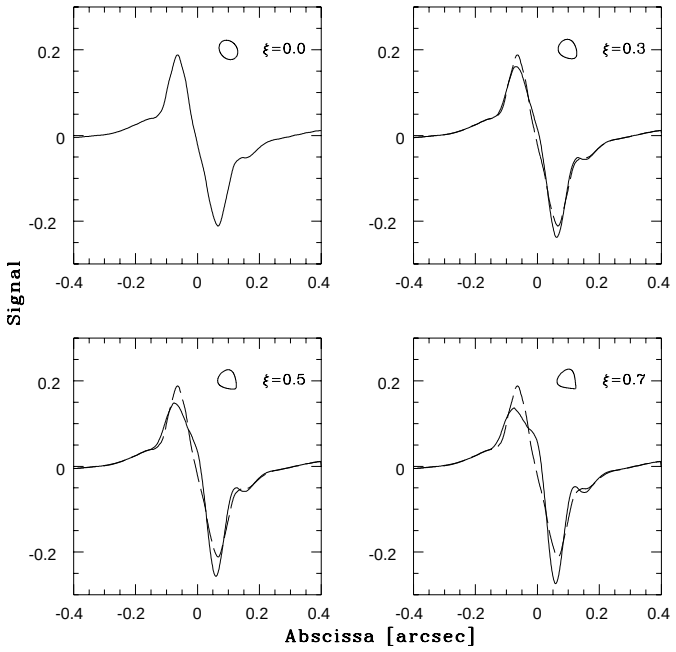

Fig. 7. Computed signal on one of the FGS axes for egg-shaped sources. The source is inclined at 45 degrees wrt the FGS axis, the apparent ellipse is 0.15 arcsec in size with a $b/a = 0.7$ flattening. The parameter ξ defines the departure to the ellipsoid figure (see text). The dashed curve corresponds to the case $\xi = 0$.

4. Data analysis

4.1. Derivation of parameters

The object intensity profile O can be retrieved from a deconvolution using Wiener filtering (Hershey 1992):

$$O \sim FFT^{-1}\left(\frac{\exp[-(f-50)/6]\,\widehat{S}(f)}{\widehat{TF}(f)}\right) \quad (5)$$

which is most often used to detect binary stars (Hershey 1992; Schneider et al. 1998; Schneider et al. 1999). This procedure is used here to provide some first hints on the size, shape and possible duplicity of the target. Later, the least-squares fit of the modeled S-curve to the observed signal is performed (Lattanzi et al. 1992, 1997).

As seen before, the observational data for a single visit provide information about the target shape projected along the two FGS axes. Let (a', b') be the sizes of the apparent ellipse; the projected size is given by $\sqrt{a'^2\cos^2\gamma + b'^2\sin^2\gamma}$, where γ is the angle between the considered FGS-axis and the semi-major axis a'. The coverage of the (u, v) spatial-frequencies-plane is limited to the two perpendicular directions of the FGS. The lowest and largest frequencies are determined by the scan-size and the sampling rate. On the other hand, the asteroid target is followed during a significant fraction of its rotational period. Hence we have typically 10 visits or "images" over approximately 30 min of the rotating body apparent-shape. The sizes of the apparent ellipse (a', b') can be related to the sizes of the ellipsoid semi-axis $a \geq b \geq c$ by functions of the (constant) aspect angle and the (varying) rotational angle. We thus distinguish two complementary steps: a single-visit fit for the data along both the FGS-X and FGS-Y axes provides a first estimate of the parameters of the model (i.e. the projected size of the object); in the second step rotational parameters and time variations are taken into account in order to reconstruct a shape capable of satisfying all visits simultaneously. During this process, as seen before, an incorrect pole solution for the spin rotation can easily be rejected. The whole procedure allows a reconstruction of the tri-axial ellipsoid size and shape, and a determination of a geometric correction to the rotational phase $\delta\lambda_{\rm SEP}$ derived from photometric light-curves.

Each step of the process consists of minimizing the squares of the residuals (non-linear least-squares) from a grid of free parameters. Assuming now that the geometry of the projected ellipse is known, the synthetic S-curve on a given FGS axis can be computed by the convolution detailed in Sect. 3.1. The main input at this stage is the semi-major axis a of the ellipsoid (with a step size of 1 mas); offsets along the abscissa and ordinate of the S-curve are also considered in the grid. The rms of the residuals that is minimized is calculated by considering only the central part of the S-curve with an arbitrary weighting function $p = 1 - (x/0.4)^2$. Such a weighting is justified because the main information on the target's shape or duplicity will be contained in the low frequencies. We now have, for each visit, the projected sizes along the two perpendicular directions of the FGS axis which are fixed on the sky. In the second step the tri-axial ellipsoid shape is fitted to this new "observational data". The free parameters are the three axis sizes and the position of the origin meridian on the asteroid surface. Again, these are determined by minimizing the rms of the residuals from a grid of the free parameters. We carry out these two-step fits iteratively until convergence is reached on the tri-axial ellipsoid parameters.

4.2. Precision and accuracy

4.2.1. Apparent ellipse – Single visit

Since the fringe pattern is derived for each scan from the photon counts I_A, I_B in the two photometers by the ratio $(I_B - I_A)/(I_B + I_A)$ (Nelan & Makidon 1999), the standard deviation $\sigma_{\rm S}$ of the signal's noise is given by:

$$\sigma_{\rm S} = \frac{2}{N}\,\frac{(I_A^2 + I_B^2)^{1/2}}{(I_A + I_B)^2}\,\sigma_{\rm I} \sim \frac{1}{\sqrt{2\,N}\,I}\,\sigma_I$$

where $I_A \sim I_B \sim I$ and $\sigma_{I_A} \sim \sigma_{I_B} \sim \sigma_I$ are function of the object's magnitude, and N (typically equal to 4) is the number of scans used for the visit. As a first approximation the noise of the – per visit – merged signal can be considered to be Gaussian: $\sigma_{\rm S} \in \mathcal{N}(0, \sigma_{\rm o})$ where the standard deviation $\sigma_{\rm o}$ is determined empirically from the data available in our HST program and we find $\sigma_{\rm o} \approx 10^{-3}\,[(V-8)^2 + 8.7]$ for $8 \leq V \leq 12$ (Table 1). To estimate the formal precision of the along-axis size determination from a single visit, we have carried out 30 best-fit calculations of the same simulated data to which a randomly varying noise was added. In this analysis two parameters were taken into account: the SNR and the object size. The dispersion of the best-fit values with respect to the known value, although larger for increasing diameter, only slightly depends on

the object size. The standard deviation is thus considered to be a function of the observation rms only (or the object magnitude). We have analyzed three classes of SNR corresponding to the magnitudes $V = 8, 10, 12$. We find that the standard deviation of the along-scan determination is in the range 0.5−1 mas on both axes. For a fainter object with $V = 15$ and $\sigma_o \sim 0.13$ the estimated along-scan standard deviation is typically of the order of 5 mas.

It is stressed that the formal precision derived here is based mainly on photon noise statistics. Inadequacy of the modeled brightness distribution (shape, spots, cratering and shadows, etc.) as well as the available template transfer functions can introduce some bias. In our case, the template that better reduces the fit residuals is chosen among those obtained from solar-type stars. To illustrate the influence of such a choice, the fit procedure was carried out with different template transfer functions. The variation on the derived along-scan sizes was of the order of 2–4 mas. While the residual can obviously reflect that the template is not adequately chosen, on the other hand it also provides some estimate of the error introduced. As a consequence the accuracy of the derived parameters for the brightest objects should be reduced. A value of 3 mas for the precision on the single-visit size determination of the brightest objects should be considered as conservative, justifying a step size of 1 mas for the fit procedure.

4.2.2. Limb-darkening

Ideally the first-step fit should provide both the along-scan size and the limb-darkening parameter. However, given the typical SNR for an object of magnitude $V \sim 10-14$, one cannot easily separate these two effects from the FGS data alone. As shown in Table 2 for a $\phi = 0.1$ arcsec large spherical object, the correlation is such that for each value of the Minnaert parameter k there exist a single value of the diameter that adequately fits the data. In other words, when simulating noised data the best-fit procedure could randomly provide a large set of possible (k, ϕ) couples. As a consequence, a uniformly bright object will be considered. Of course, once again, we stress here that the derived sizes are model-dependent, not differently to other methods used until now. Adopting a stronger limb-darkening would provide larger sizes, the bias being however smaller when the ellipsoid flattening is large.

4.2.3. Tri-axial ellipsoid – multi visit

Next, to estimate the formal precision of the asteroid size and shape determination from the total number of visits (the pole coordinates being fixed), we have again constructed simulated size sets – two values (FGS-X and FGS-Y) for each visit – with randomly varying noise. However the errors on the determined ellipsoid parameters strongly depend on the asteroid geometry during the observation, hence a general relation valid for any asteroid and at any date cannot be provided. A particular configuration can however give some interesting estimates for different situations.

Table 2. Limb-darkening and diameter correlation for a spherical body.

Minnaert k	Diameter ϕ [arcsec]	rms $\times 10^{-4}$
U.B.[a]	0.100	4
0.6	0.109	13
0.7	0.110	14
0.8	0.111	15
0.9	0.113	17
1.0	0.114	17

[a] Values when considering a uniform brightness are given for comparison.

We choose an ellipsoidal body having sizes $a = 50$, $b = 30$, $c = 40$ mas, having the c axis parallel to the FGS-Y direction. The object is assumed to be in equatorial view and observed for half an hour, resulting in 10 visits (i.e. of 10 projected sizes for each FGS axis). As a consequence, the projection of c is coincident with c itself, and being also parallel to the rotation axis, it does not vary with time. The projection of a is always parallel to the FGS-X directions, but it changes its size. The origin of rotation is chosen in such a way that it passes by the position of the "ideal" projection during the observation. The b axis, having a projection strongly shortened, is the most poorly observed one in this case. Given this geometry, a set of projected sizes with Gaussian noise (with $\sigma = 1$ mas) was produced. A least-squares determination of a, b, c, and the rotational phase was then run. The whole procedure was repeated for 60 different noise realizations.

The results show that typical standard deviations for each determination of the four parameters above are the following: $\sigma_a = 0.21$ mas, $\sigma_b = 4.84$ mas, $\sigma_c = 0.15$ mas, $\sigma_{\rm long} = 1.56$ degrees. These values can be taken as significant for very well projected (a and c) axis, and for very poorly constrained (b) ones. Of course, this ideal situation (eliminating all possible interference of albedo inhomogeneities, poorly determined rotational poles, etc.) cannot capture all the complexity of real cases. Anyway, we can consider it to be a good indication of the high robustness and of the formal accuracy of the procedure adopted.

Of course, in real cases, the presence of complex surface effects not considered here could allow one to reach this high accuracy only if the complex effects could be satisfactorily taken into account by the model, i.e. only if a sufficiently rich set of observations (possible at different geometries) is available.

5. Conclusion

This work shows that HST observations using the FGS astrometer are of great value not only to resolve moderately extended objects, but also to determine the size and shape of asteroids, to reject wrong pole solutions and to reveal nearly-contact binary asteroids. Results should even be enhanced with the upgraded and more sensitive FGSR#1. On the other hand it is clear that observations at – at least – two different epochs and aspect

angles are necessary to completely define the ellipsoid shape of an asteroid or a binary system; and that the full rotation period must be covered in order to detect any shape or albedo deviation from the ellipsoidal model. A procedure to determine a tri-axial ellipsoid model (for a single object as well as for a binary structure) has been constructed here, but it should be mentioned that the HST/FGS is also a platform well-suited to test or improve 3-dimensional shape models of asteroids obtained by other techniques.

Acknowledgements. We are grateful to the FGS team at the STScI in particular E. Nelan and D. C. Taylor. D. Hestroffer acknowledges funding from the OATo. We also thank D. Loreggia for work during part of the data reduction and J. Laskar for providing of computing facilities.

Appendix A: Analytical expression of the *S*-curve

Neglecting instrumental aberration and off-centering, the transfer function for a point source can roughly be evaluated analytically by (Loreggia 1997):

$$T(x) = \int_{t=0}^{R} \int_{\lambda=400}^{800} S\,p(\lambda)\,\sin(2\,k\,t\,x)\,\mathrm{d}t\,\mathrm{d}\lambda \tag{A.1}$$

where $S\,p(\lambda)$ is the target spectral response at the receptor, $k = 2\,\pi/\lambda$, and R is the primary-mirror radius. For an extended source the signal is given by:

$$S(x) = \int_{t}\int_{\lambda} |U(t)|\,S\,p(\lambda)\,\sin(2\,k\,t\,x)\,\mathrm{d}t\,\mathrm{d}\lambda \tag{A.2}$$

where $|U(t)|$, the spatial correlation function of the source $\mathcal{S}$, is derived from the Zernike-Van Cittert theorem by the Fourier transform:

$$U(t) = \frac{\iint_{\mathcal{S}} I(u,v)\ \exp[-2\,j\,k\,t\,u]\,\mathrm{d}u\,\mathrm{d}v}{\iint_{\mathcal{S}} I(u,v)\,\mathrm{d}u\,\mathrm{d}v}\cdot \tag{A.3}$$

If both the source and its brightness distribution are radially symmetric ($I = I_\mathrm{r}$) the spatial correlation is deduced from the Hankel transform of zero order of the function I_r.

$$U(t) = \frac{\displaystyle\int_0^1 r\,I_\mathrm{r}\,\left\{\int_0^{2\pi} \exp[-2\,j\,k\,t\,\rho\,r\,\cos\theta]\,\mathrm{d}\theta\right\}\,\mathrm{d}r}{\displaystyle\iint_{\mathcal{S}} I_\mathrm{r}\,r\,\mathrm{d}r\,\mathrm{d}\theta} \tag{A.4}$$

where ρ is the apparent radius of the source. If the light distribution follows a power law of the form $I_\mathrm{r} = \mu^{2(\nu-1)} = (1-r^2)^{(\nu-1)}$ where $\nu \in \mathbb{R}$, the spatial correlation is given by the generalized hypergeometric function (Hestroffer 1997):

$$|U(t)| = \left|{}_0F_1\left(\nu+1; -(k\,\rho\,t)^2\right)\right|\cdot \tag{A.5}$$

In the special case where a star has a circular disc of uniform intensity, we have $\nu = 1$ and the well-known result $|U(t)| = 2\,|J_1(k\,\rho\,t)|/(k\,\rho\,t)$, where J_1 is the Bessel function of the first kind. For a monochromatic source or a narrow filter of wavelength $\bar{\lambda}$ we have:

$$S(x) = S\,p(\bar{\lambda}) \int_{t=0}^{R} \left|{}_0F_1\left(\nu+1; -(\bar{k}\,\rho\,t)^2\right)\right| \sin\left(2\,\bar{k}\,t\,x\right)\,\mathrm{d}t \tag{A.6}$$

where the abscissa x is in radians.

Appendix B: Expressions for the synthetic *S*-curve

The observed S-curve can be expressed by the convolution of the signal of a point-like source with the target 2D brightness distribution. For a sphere $\mathcal{S}$ of radius ρ it can be best written in spherical coordinates (λ, β). Introducing the surface element $\mathrm{d}\sigma = \cos\beta\,\mathrm{d}\lambda\,\mathrm{d}\beta$, and the cosines between the surface normal and the incident ray (μ_o) and reflected ray (μ), we have:

$$\begin{aligned}
\mu &= \cos\beta\cos\lambda \\
\mu_\mathrm{o} &= \cos\beta\cos(\lambda+\alpha) \\
X &= x - \rho\cos\beta\sin\lambda\cos\gamma + \rho\sin\beta\sin\gamma
\end{aligned}$$

$$S(x) = \frac{\iint_{\mathcal{S}} I(\mu,\mu_o)\ T(X)\ \mu\,\mathrm{d}\sigma}{\iint_{\mathcal{S}} I(\mu,\mu_o)\ \mu\,\mathrm{d}\sigma} \tag{B.1}$$

where γ is the orientation of the FGS axis with respect to the intensity equator, and $I(\mu,\mu_\mathrm{o})$ is the target's brightness distribution (including possible albedo spots).

Moreover, when the brightness distribution is radially symmetric it can be written in polar coordinates, and we have for any orientation of the FGS axis:

$$S(x) = \frac{\displaystyle\int_0^{\rho}\int_0^{2\pi} I(r)\ T(x - r\,\cos\theta)\ r\,\mathrm{d}r\mathrm{d}\theta}{\displaystyle\iint_{\mathcal{D}} I(r)\ r\,\mathrm{d}r\mathrm{d}\theta}\cdot \tag{B.2}$$

Starting from Eq. (B.1) and making use of the affine transformation:

$$\left|\begin{array}{rcl} X &=& \rho\,\cos\beta\cos\lambda \\ Y &=& (b/a)\,\rho\,\cos\beta\sin\lambda \\ Z &=& (c/a)\,\rho\,\sin\beta \end{array}\right. \tag{B.3}$$

we also obtain the observed signal for a tri-axial ellipsoid target. Projection in the focal plane yields:

$$S(x) = \frac{\iint_{\mathcal{E}} I(u,v)\ T(x - u\cos\gamma + v\sin\gamma)\,\mathrm{d}u\,\mathrm{d}v}{\iint_{\mathcal{E}} I(u,v)\,\mathrm{d}u\,\mathrm{d}v} \tag{B.4}$$

where the bounding of the apparent-ellipse visible part $\mathcal{E}$ as well as the position angle γ of the FGS axis with respect to the apparent ellipse major axis are deduced from the computed

physical ephemeris. The expression obtained for a binary object is straightforward, for the sake of brevity we give it for the special case $\gamma = 0$:

$$A(x) = \iint_{\mathcal{E}_A} I_A(u,v)\, T(x-u)\, \mathrm{d}u\, \mathrm{d}v$$

$$B(x) = \iint_{\mathcal{E}_B} I_B(u,v)\, T(x-\delta-u)\, \mathrm{d}u\, \mathrm{d}v$$

$$S(x) = \frac{A(x) + B(x)}{\iint_{\mathcal{E}_A} I_A(u,v)\, \mathrm{d}u\, \mathrm{d}v + \iint_{\mathcal{E}_B} I_B(u,v)\, \mathrm{d}u\, \mathrm{d}v} \quad \text{(B.5)}$$

where δ is the components' center-to-center algebraic separation projected on the sky and on the FGS axis, and is deduced from the computed physical ephemeris.

Appendix C: Effect of flattening

The observed signal is given for an apparent ellipse $\mathcal{E}$ of semi-major axis a by the convolution:

$$S(x) = \frac{\iint_{\mathcal{E}} I(u,v)\, T(x - u\cos\gamma + v\sin\gamma)\, \mathrm{d}u\, \mathrm{d}v}{\iint_{\mathcal{E}} I(u,v)\, \mathrm{d}u\, \mathrm{d}v} \quad \text{(C.1)}$$

where $T(x)$ is the template transfer function, $I(u,v)$ the object brightness distribution, and γ the position angle of the major axis with respect to the FGS axis. Making use of the transformation:

$$\begin{vmatrix} U &= & (u\cos\gamma - v\sin\gamma)\,(\cos^2\gamma + \zeta^2\sin^2\gamma)^{1/2} \\ V &= \zeta^{-1} & (u\sin\gamma + v\cos\gamma)\,(\cos^2\gamma + \zeta^2\sin^2\gamma)^{1/2} \end{vmatrix} \quad \text{(C.2)}$$

where $\zeta = b/a$ is the flattening of the ellipse, we have:

$$S(x) = \frac{\iint_{\mathcal{D}} I(u,v)\, T(x-U)\, \mathrm{d}U\, \mathrm{d}V}{\iint_{\mathcal{D}} I(u,v)\, \mathrm{d}U\, \mathrm{d}V} \quad \text{(C.3)}$$

which is the observed signal for a disk $\mathcal{D}$ of radius $R = a\,(\cos^2\gamma + \zeta^2\sin^2\gamma)^{1/2}$. The expressions of $u = f(U,V)$ and $v = g(U,V)$ are straightforward but not given here. We conclude that: if the effect of aberration can be neglected over a radius of $\approx$0.2 arcsec, then the signal for a flattened disk of semi-major axis $a \lesssim 0.2$ arcsec is equal to the signal of the sphere of radius $R = a\,(\cos^2\gamma + \zeta^2\sin^2\gamma)^{1/2}$ with the same brightness distribution (i.e. $I(u,v) = I(U,V)$). It is stressed that this result is limited by the brightness distribution since the sphere and the ellipsoid that are connected by an affine transformation will not follow the same physical or empirical brightness distribution. The signals will be slightly different when the brightness distribution depends on the normal to the surface element (e.g., Minnaert et al. 1983 scattering laws).

References

André, C. 1901, Astron. Nachr., 155, 27
Arlot, J. E., Lecacheux, J., Richardson, C., & Thuillot, W. 1985, Icarus, 61, 224
Belton, M., & Carlson, R. 1994, IAU Circ., 5948
Benner, L. A. M., Hudson, R. S., Ostro, S. J., et al. 1999, Icarus, 139, 309
Bernacca, P. L., Lattanzi, M. G., Bucciarelli, B., et al. 1993, A&A, 278, L47
Bernacca, P. L., Lattanzi, M. G., Porro, I., Neuhaeuser, R., & Bucciarelli, B. 1995, A&A, 299, 933
Bottke, W. F., & Melosh, H. J. 1996, Icarus, 124, 372
Bowell, E., McMahon, J., Horne, K., et al. 1978, Bull. Amer. Astron. Soc., 10, 594
Buratti, B., & Veverka, J. 1983, Icarus, 55, 93
Cellino, A., Pannunzio, R., Zappalà, V., Farinella, P., & Paolicchi, P. 1985, A&A, 144, 355
Chapman, C. R., Veverka, J., Thomas, P. C., et al. 1995, Nature, 374, 783
Chauvineau, B., Mignard, F., & Farinella, P. 1991, Icarus, 94, 299
Cook, A. F. 1971, in Physical Studies of Minor Planets, IAU Colloq., 12, 155
Doressoundiram, A., Paolicchi, P., Verlicchi, A., & Cellino, A. 1997, Planet. Space Sci., 45, 757
Durda, D. D. 1996, Icarus, 120, 212
Farinella, P., & Chauvineau, B. 1993, A&A, 279, 251
Farinella, P., Paolicchi, P., & Zappalà, V. 1981, A&A, 104, 159
Farinella, P., Paolicchi, P., & Zappalà, V. 1982, Icarus, 52, 409
Franz, O. G., Kreidl, T. J. N., Wasserman, L. W., et al. 1991, ApJ, 377, L17
Franz, O. G., Wasserman, L. H., Nelan, E., et al. 1992, AJ, 103, 190
Gehrels, T., Drummond, J. D., & Levenson, N. A. 1987, Icarus, 70, 257
Gradie, J., & Flynn, L. 1988, Lunar Planetary Sci. Conf., 19, 405
Hamilton, D. P., & Burns, J. A. 1992, Icarus, 96, 43
Hartmann, W. K. 1979, in Lunar and Planetary Sci. Conf., 10th, Houston, Tex., March 19–23, 1979, vol. 10 (New York, Pergamon Press, Inc.), 1897
Hershey, J. L. 1992, PASP, 104, 592
Hestroffer, D. 1997, A&A, 327, 199
Hoffmann, M. 1991, Astron. Nach., 312, 201
Hook, R. N., Schreier, E. J., & Miley, G. 2000, ApJ, 536, 308
Hudson, R. S., & Ostro, S. J. 1994, Science, 263, 940
Lattanzi, M. G., Bucciarelli, B., Holfeitz, S. T., & Taff, L. G. 1992, in ASP Conf. Ser. 32, IAU Colloq. 135, Complementary Approaches to Double and Multiple Star Research, 377
Lattanzi, M. G., Hershey, J. L., Burg, R., et al. 1994, ApJ, 427, L21
Lattanzi, M. G., Munari, U., Whitelock, P. A., & Feast, M. W. 1997, ApJ, 485, 328
Leone, G., Paolicchi, P., Farinella, P., & Zappalà, V. 1984, A&A, 140, 265
Loreggia, D. 1997, Ph.D. Thesis, Turin observatory, Italy
Magnusson, P., Lagerkvist, C., Dahlgren, M., et al. 1994, in Asteroids, Comets, Meteors 1993, IAU Symp., 160, 471
Marchis, F., Hestroffer, D., Cellino, A., Tanga, P., & Zappalà, V. 1999, IAU Circ., 7308
Martelli, G., Rothwell, P., Giblin, I., et al. 1993, A&A, 271, 315
Merline, W. J., Close, L. M., Dumas, C., et al. 1999, Nature, 401, 565
Merline, W. J., Close, L. M., Dumas, C., et al. 2000, AAS/Division Planet. Sci. Meet., 32, 1306
Michel, P., Benz, W., Tanga, P., & Richardson, D. C. 2001, Science, 294, 1696

Mineur, H. 1952, Techniques de calcul numérique (Paris-Liège: Librairie polytechnique Ch. Béranger)
Minnaert, M. 1941, ApJ, 93, 403
Monet, A. K. B., & Monet, D. G. 1998, AAS/Division Dyn. Astron. Meet., 30, 0802
Mottola, S., & Lahulla, F. 2000, Icarus, 146, 556
Nelan, E. P., Lupie, O. L., McArthur, B., et al. 1998, Proc. SPIE, 3350, 237
Nelan, E. P., & Makidon, R. 1999, FGS Instrument Handbook, version 8.0 (Baltimore, USA: STSci)
Ostro, S. J. 1993, Amer. Astron. Soc. Meet., 182, 2401
Ostro, S. J., Chandler, J. F., Hine, A. A., et al. 1990, Science, 248, 1523
Ostro, S. J., Hudson, R. S., Nolan, M. C., et al. 2000, Science, 288, 836
Pravec, P., Wolf, M., & Sarounova, L. 1998, Icarus, 133, 79
Richardson, D. C., Leinhardt, Z. M., & Quinn, T. 1999, AAS/Division Planet. Sci. Meet., 31, 3302
Roberts, L. C., McAlister, H. A., Hartkopf, W. I., & Franz, O. G. 1995, AJ, 110, 2463
Schneider, G., Hershey, J. L., & Nelan, E. 1999, Amer. Astron. Soc. Meet., 195, 75.16
Schneider, G., Hershey, J. L., & Wenz, M. T. 1998, PASP, 110, 1012
Storrs, A., Weiss, B., Zellner, B., et al. 1999, Icarus, 137, 260
Tanga, P., Hestroffer, D., Berthier, J., et al. 2001, Icarus, 153, 451
Tanga, P., Hestroffer, D., Cellino, A., et al. in prep., Asteroids observations with the Hubble Space Telescope II, A&A, submitted
Tanga, P., Loreggia, D., Hestroffer, D., et al. 1999, AAS/Division Planet. Sci. Meet., 31, 20.03
Tedesco, E. F. 1979, Science, 203, 905
van Flandern, T. C., Tedesco, E. F., & Binzel, R. P. 1979, in Asteroids, 443
Weidenschilling, S. J. 1980, Icarus, 44, 807
Weidenschilling, S. J., Paolicchi, P., & Zappalà, V. 1989, in Asteroids II, 643
Zappalà, V., di Martino, M., Scaltriti, F., Djurasevic, G., & Knezevic, Z. 1983, Icarus, 53, 458